Journal of Magnetic Resonance Open 21 (2024) 100172

Contents lists available at ScienceDirect

Journal of Magnetic Resonance Open

journal homepage: www.sciencedirect.com/journal/journal-of-magnetic-resonance-open

Research article

Hyperpolarization and sensitivity in nuclear magnetic resonance

Karel Kouřil [a], Benno Meier [a,b,*]

[a] Institute of Biological Interfaces 4, Karlsruhe Institute of Technology, Herrmann-von-Helmholz-Platz 1, 76344 Eggenstein-Leopoldshafen, Germany
[b] Institute of Physical Chemistry, Karlsruhe Institute of Technology, Fritz-Haber-Weg 2, 76131 Karlsruhe, Germany

ARTICLE INFO

Dataset link: https://doi.org/10.35097/st1kjwpvsce77dhw

Keywords:
Hyperpolarization
Sensitivity
Signal-to-noise
Brillouin-function
Q-factor

ABSTRACT

Hyperpolarization can boost the sensitivity of nuclear magnetic resonance. Other things being equal, a polarization increase by one order of magnitude leads to a time saving by two orders of magnitude. However, other things are rarely equal, and in this tutorial article we calculate how side effects of hyperpolarization, namely changes in duty cycle, dilution, and resolution, influence the net sensitivity and time savings of the (hyperpolarized) NMR experiment. The signal-to-noise ratio is calculated both in time- and frequency-domain for a sample at thermal equilibrium using the principle of reciprocity. The hyperpolarized time gain (HYTIGA) is calculated separately for concentration- and mass-limited samples. The article includes a detailed appendix on the measurement of the coil's Q-factor.

1. Introduction

Put simply, the objective of hyperpolarization is to gather information of a quality or quantity that cannot easily be collected without hyperpolarization.

The most widely used hyperpolarization methods increase the normally available thermal polarization by using low temperatures, larger interactions than the nuclear spin interactions, or a combination of these two means. In brute-force hyperpolarization, a hyperpolarized nuclear spin state is attained at ambient temperature by first equilibrating the nuclear spins at high field and low temperature [1,2]. In Overhauser-dynamic nuclear polarization (DNP), the larger electron Zeeman interaction gives rise to a strong electron spin polarization. If a suitable electron–nuclear cross-relaxation mechanism is active, this polarization may be transferred to nuclear spins by saturating the electron spin transition [3–6]. In magic angle spinning (MAS) DNP, as well as in dissolution-DNP, the electron spin polarization is boosted further by polarizing the electron spins at low temperature. The polarization transfer to the nuclei occurs either by strong microwave irradiation of a forbidden electron–nuclear transition (the solid effect), or by saturating parts of the EPR spectrum in such a way that ensuing electron–electron–nuclear triple-spin–flips drive the nuclear spin polarization towards a negative minimum or a positive maximum. Similarly, in parahydrogen-induced polarization, one uses a combination of a large interaction (the rotational splitting of dihydrogen) and low temperatures to create a highly ordered spin state from which hyperpolarization can be derived.

Non-equilibrium spin hyperpolarization may also be derived from other techniques, such as spin-selective chemical reactions [7], polarized light [8], or light-induced radical pairs [9–12]. A comprehensive review of spin hyperpolarization techniques has recently been presented by Eills, Koptyug and co-workers [13].

The departure from thermal equilibrium may be rewarded with a high polarization, but the gain in sensitivity is often much smaller than the gain in polarization. In this tutorial, we describe how nuclear spins, either at thermal equilibrium or hyperpolarized, give rise to a nuclear magnetization. The precession of this magnetization induces a voltage in the NMR coil. The coupling of the magnetization to the NMR coil is discussed in terms of the principle of reciprocity. In addition to the induced voltage, the random motion of electrons in the coil wire produces a noise voltage. A Fourier transform of the time-dependent voltage produces the NMR spectrum, and the signal-to-noise ratio is the maximum of the spectral line due to the precessing magnetization, divided by the root mean square of the noise in the spectrum.

The sensitivity of an NMR experiment is the attainable signal-to-noise ratio for a specified concentration or mass of nuclear spins and a specified time. We introduce the *hyperpolarized time gain* (HYTIGA), which measures how much time can be saved (or wasted) using hyperpolarization. The application of hyperpolarization is useful when HYTIGA $\gg 1$, and this is typically the case when observing short-lived intermediates, or systems where the analyte concentration is dictated by the application and not by the hyperpolarization process. For mass-limited samples on the other hand the time gain is highly sensitive to

* Corresponding author at: Institute of Biological Interfaces 4, Karlsruhe Institute of Technology, Herrmann-von-Helmholz-Platz 1, 76344 Eggenstein-Leopoldshafen, Germany.
E-mail address: benno.meier@kit.edu (B. Meier).

https://doi.org/10.1016/j.jmro.2024.100172
Received 21 July 2024; Received in revised form 28 October 2024; Accepted 6 November 2024
Available online 16 November 2024

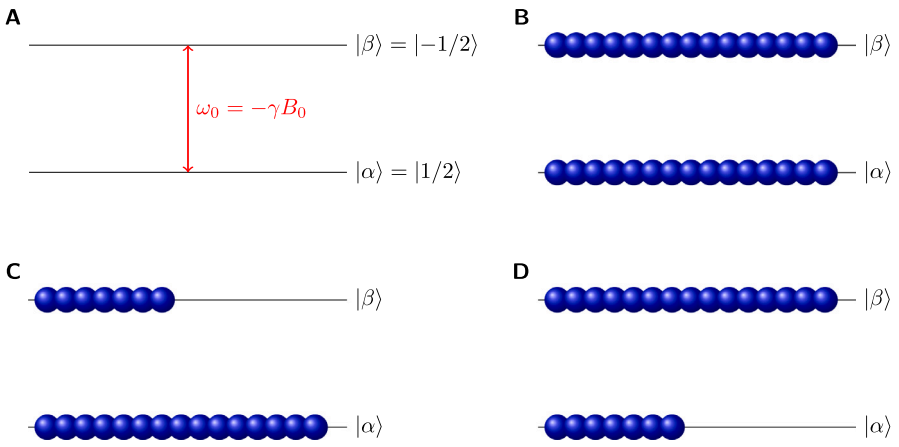

Fig. 1. (**A**) The Zeeman interaction gives rise to a splitting between the nuclear spin states of an ensemble of spins 1/2. (**B**) The splitting is typically weak compared to the available thermal energy, and so the spin states are populated almost equally. (**C**) and (**D**) show ensembles with a large positive and a large negative polarization, respectively.

the detector volume and Q-factor, and may be smaller than 1 even for highly polarized spins. Separate HYTIGA expressions are given for mass- and concentration-limited samples. A detailed appendix derives procedures for the measurement of circuit Q.

2. Polarization

The interaction of the nuclear magnetic moment $\boldsymbol{\mu}$ with an applied magnetic field $\boldsymbol{B}$ is the Zeeman interaction:

$$E = -\boldsymbol{\mu} \cdot \mathbf{B}. \tag{1}$$

The magnetic moment is parallel to the nuclear angular momentum $\boldsymbol{J}$,

$$\boldsymbol{\mu} = \gamma \boldsymbol{J} = \gamma \hbar \langle \boldsymbol{I} \rangle \tag{2}$$

where γ is the gyromagnetic ratio of the given nucleus, $\boldsymbol{I} = (\hat{I}_x, \hat{I}_y, \hat{I}_z)$ is a dimensionless angular momentum or spin operator, and $\langle \ldots \rangle$ denote the expectation value of the respective operator.

We choose to apply our magnetic field along the z axis, i.e. $\boldsymbol{B} = (0, 0, B_0)^T$ and obtain

$$E = -\gamma \hbar \left\langle \hat{I}_z \right\rangle B_0 \tag{3}$$

Typically, the Zeeman interaction dominates all other interactions. The eigenvalues of $\hat{I}_z$ are then good quantum numbers in the sense that they describe the stationary states of the spins. The eigenvalues of $\hat{I}_z$ are $m_z = -I, -I+1, \ldots, I$, where I is the spin of the nucleus under consideration, and one obtains the energy structure shown in Fig. 1.

Much like earth's magnetic field aligns the magnetic moment of a compass needle, a magnetic field tends to align nuclear spins. Using Slichter's analogy [14], without friction a compass needle would oscillate about the earth's field indefinitely. The friction processes that lead to alignment in NMR are T_1 processes. It is by these processes, that after a time of the order of T_1, a thermal equilibrium is established. The thermal equilibrium is described by a Boltzmann distribution.

2.1. Polarization for an ensemble of spins 1/2

For spins 1/2, like ^{1}H, ^{13}C and the electron, the two eigenvalues of $\hat{I}_z$ are $m_z = \pm 1/2$. We use the symbol $|\alpha\rangle$ for the $m_z = 1/2$ ground state, and the symbol $|\beta\rangle$ for the higher energy state with $m_z = -1/2$, and denote the populations of these two states with $p_{|\alpha\rangle}$ and $p_{|\beta\rangle}$, respectively. The sum of the populations is equal to one: $p_{|\alpha\rangle} + p_{|\beta\rangle} = 1$.

The polarization is then defined as the difference of the populations of the two states:

$$P = p_{|\alpha\rangle} - p_{|\beta\rangle} = 1 - 2p_{|\beta\rangle}. \tag{4}$$

After thermal equilibrium is established, i.e. after $3 - 5T_1$, the ratio of the two populations is described by the Boltzmann distribution.

$$\frac{p_{|\beta\rangle}}{p_{|\alpha\rangle}} = \exp\left(-\frac{\hbar\gamma B_0}{kT}\right) =: \mathcal{B} \tag{5}$$

where T is the lattice (e.g. sample) temperature, and where we have introduced the Boltzmann ratio $\mathcal{B}$. Solving the above equation for $p_{|\beta\rangle}$ gives

$$p_{|\beta\rangle} = (1 - p_{|\beta\rangle})\mathcal{B} \tag{6}$$

$$= \frac{\mathcal{B}}{1+\mathcal{B}} = \frac{1}{1+\mathcal{B}^{-1}} \tag{7}$$

and, with $x = \hbar\gamma B/(kT)$, we obtain the well-known result

$$P = 1 - 2p_{|\beta\rangle} = 1 - \frac{2}{1+\mathcal{B}^{-1}} = \frac{\mathcal{B}^{-1} - 1}{\mathcal{B}^{-1} + 1} \tag{8}$$

$$= \frac{\exp\left(\frac{2x}{2}\right) - 1}{\exp\left(\frac{2x}{2}\right) + 1} = \tanh\left(\frac{x}{2}\right) = \tanh\left(\frac{\hbar\gamma B}{2kT}\right), \tag{9}$$

Using this result, we show the polarization for ^{1}H, ^{13}C and the electron as a function of temperature at a field of 6.7 T in Fig. 2.

2.2. Polarization for an ensemble of spins > 1/2

In general, the nuclear spin may be > 1/2. The general definition of the spin polarization is

$$P = \frac{1}{I}\left\langle \hat{I}_z \right\rangle. \tag{10}$$

In thermal equilibrium,

$$\left\langle \hat{I}_z \right\rangle = \sum_{m_I=-I}^{I} m_I p_{m_I} \tag{11}$$

Now we shift indices and make use of the fact that the ratio of the populations of two adjacent levels is given by $\mathcal{B}$.

$$\left\langle \hat{I}_z \right\rangle = \sum_{j=0}^{2I} m_{I-j} p_j = \sum_{j=0}^{2I} m_{I-j} p_G \mathcal{B}^j \tag{12}$$

Herein, the symbol p_G denotes the population of the ground state. Again, the sum of all populations is equal to one:

$$p_G(\mathcal{B}^0 + \mathcal{B}^1 + \mathcal{B}^2 + \cdots + \mathcal{B}^{2I}) = 1 \Rightarrow p_G = 1/\sum_{j=0}^{2I} \mathcal{B}^j. \tag{13}$$

Combining this result with (10) and (12) gives

$$P = \frac{1}{I} \frac{\sum_{j=0}^{2I} m_{I-j} \mathcal{B}^j}{\sum_{j=0}^{2I} \mathcal{B}^j} \tag{14}$$

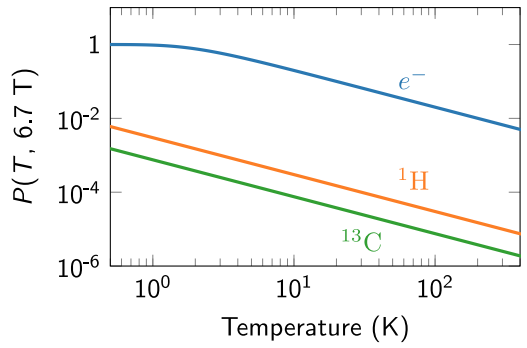

Fig. 2. Polarization for a free electron spin, protons and carbons at 6.7 T and for temperatures between 0.5 and 400 K. For the nuclear spins, the high-temperature approximation is valid across the shown temperature range. The electron has near unity polarization at 1 K.

$$= \frac{2I+1}{2I}\coth\left(\frac{2I+1}{2}x\right) - \frac{1}{2}\coth\left(\frac{1}{2}x\right) = B_I(Ix) \tag{15}$$

The function B_I is called the Brillouin function, the derivation is given in Appendix A. Eq. (14) is the general expression for the polarization of any spin at any temperature, provided that it is quantized along the applied magnetic field. The Brillouin function is the appropriate expression for paramagnetic ions such as Gd^{3+} at low temperatures and high magnetic fields [15], but also for quadrupolar nuclei with near unity polarization. The only spin systems where this formula cannot be applied are nuclei with a quadrupolar interaction that is significant compared to the Zeeman interaction and electron spins with g-anisotropy of the order of unity [16]. We note that the same result for the polarization is obtained using the thermal equilibrium density matrix ρ_{th}, and the expectation value $\langle \hat{I}_z \rangle = \mathrm{Tr}\{\rho \hat{I}_z\}$.

2.3. The high-temperature approximation

When $x = \hbar\gamma B_0/kT \ll 1$, we can approximate $\mathcal{B} \approx 1 - x$. For the powers of $\mathcal{B}$ we furthermore have $\mathcal{B}^j \approx (1-x)^j \approx 1 - jx$. With $m_{I-j} = I - j$, the expression for the polarization then becomes

$$P \approx \frac{1}{I}\frac{\sum_{j=0}^{2I}(I-j)(1-jx)}{\sum_{j=0}^{2I}(1+jx)}. \tag{16}$$

The sum over $(I-j)1$ in the numerator vanishes, so that only the sum over $(I-j)jx$ contributes. In the denominator we ignore the small contribution from jx, and the remaining sum over 1 gives $2I+1$. We then get

$$P \approx \frac{x(I+1)}{3} = \frac{\hbar\gamma B_0(I+1)}{3kT} \tag{17}$$

This is the high-temperature approximation.

2.4. Spin temperature

The thermal equilibrium spin polarization is a monotonic function of temperature. For spins 1/2, we can therefore describe any spin polarization P_0 using a spin temperature. Following a perturbation, e.g. by an RF pulse, a spin system cannot be described by a spin temperature. Then it is often sufficient to wait for T_2 relaxation processes to complete before the spin temperature is well-defined. In terms of the density matrix this statement is equivalent to saying that any off-diagonal elements or coherences need to vanish for a spin temperature to be defined. The T_1 processes on the other hand describe how the spin temperature returns to its thermal equilibrium value, or, in other words, the lattice temperature.

If the spin polarization differs from the thermal equilibrium polarization, the spin temperature will differ from the lattice temperature. To find the spin temperature, for spins 1/2 we can always choose T such that $P(T) = P_0$. It turns out that this spin temperature has a physical significance. In solid samples, the nuclear spins of one species form a thermal reservoir that can exchange heat with nuclear spins of a different species. The coupling between the two reservoirs depends greatly on the field strength, as well as whether radicals are present in the sample. If the coupling is strong (as is the case in the presence of wideline nitroxide radicals), different nuclei will tend to attain the same spin temperature [1,17–20]. Note that the polarization of the different nuclei will not be the same due to the appearance of γ in the conversion between spin temperature and polarization.

2.5. Polarization and order

A highly polarized spin system has a high degree of spin order, but a highly ordered spin system does not necessarily have a high polarization. Consider an ensemble of spin 1 nuclei where all nuclei are in the $m = 0$ state. This is a highly ordered spin system, yet the expectation value of $\hat{I}_z$, and therefore the polarization are 0. A similar example is pure parahydrogen which is also highly ordered and likewise has a vanishing polarization. A quantitative measure of the order of a spin system is its entropy, and it has recently been suggested to use entropy as a measure of spin order [21].

Alternatively, the order of nuclear spins with $I \geq 1$ may be described using polarization tensors. This approach is presented briefly in Appendix B.

Here, we prefer to use the conventional definition of polarization, which ensures that the magnetization is proportional to the polarization.

3. Magnetization

The NMR signal is induced in the NMR coil by the precessing nuclear spin magnetization. The magnetization is defined as magnetic moment per unit volume, with units of A/m. The magnetic moment is the expectation value of $\boldsymbol{\mu}$. We denote the spin density, i.e. (the number of spins $\mathcal{N}$ per volume V) with $n = \mathcal{N}/V$. Of course, n is related to the molar concentration c by $n = cN_A 1000\mathrm{L/m}^3$. After complete relaxation, the magnetization will only be non-zero along the z axis:

$$M_z = n\gamma\hbar\langle \hat{I}_z \rangle = n\gamma\hbar I P \tag{18}$$

where P is given by Eq. (14).

In the case of an arbitrary spin in the high-temperature limit we use (17), and have

$$M_z = n\gamma\hbar I\frac{\hbar\gamma B_0(I+1)}{3kT}. \tag{19}$$

This equation is known as the Curie law.

4. The NMR signal

A radio-frequency (RF) pulse is now required to generate the transverse magnetization that gives rise to the NMR signal. We assume that the RF pulse is a perfect 90 degree pulse, so that the transverse magnetization M_x *after* the pulse will be equal to the longitudinal magnetization M_z *before* the pulse. The magnetization will precess about the magnetic field with the Larmor frequency ω. Faraday's law of induction states that the voltage $\tilde{V}$ induced in a coil with N_t turns by a changing flux Φ is

$$\tilde{V} = -N_t\frac{\mathrm{d}\Phi}{\mathrm{d}t}. \tag{20}$$

The flux Φ is given as the magnetic field B flowing through the coil, multiplied with its cross-section A. The magnetic field in turn is given by $B = \mu_0 M$. If we assume M to precess according to $M_x = M_z\cos(\omega t)$, we have

$$\tilde{V} = N_t A\mu_0\omega M_z\sin(\omega t) \tag{21}$$

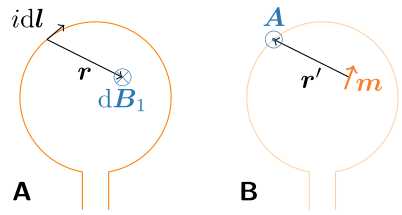

Fig. 3. The principle of reciprocity. (**A**) A current i flowing along a segment of coil wire $\mathrm{d}\boldsymbol{l}$ generates a magnetic field $\mathrm{d}\boldsymbol{B}_1$ at a distance $\boldsymbol{r}$ from the coil segment. (**B**) A magnetic moment $\boldsymbol{m}$ at this point generates a vector potential $\boldsymbol{A}$ at the point of the coil segment, with $\boldsymbol{r}' = -\boldsymbol{r}$.

For a sample with thermal equilibrium polarization, the induced voltage scales as $\gamma^3 B_0^2 I(I+1)$.

Before we turn to the time dependence of the NMR signal, we consider the influence of the coil geometry on the attainable signal amplitude. The first puzzle piece is the famous principle of reciprocity, introduced into the NMR community by Hoult and Richards [22].

Consider a current i running through a coil as shown in Fig. 3 A. The magnetic field $\mathrm{d}\boldsymbol{B}_1$ generated by the length element $\mathrm{d}\boldsymbol{l}$ at a point $\boldsymbol{r}$ away from $\mathrm{d}\boldsymbol{l}$ is given by Biot–Savart's law as

$$\mathrm{d}\boldsymbol{B}_1(\boldsymbol{r}) = \frac{\mu_0}{4\pi}\frac{i\mathrm{d}\boldsymbol{l}\times\boldsymbol{r}}{r^3} \tag{22}$$

If we take the integral along the entire wire W, we get

$$\boldsymbol{B}_1(\boldsymbol{r}) = \frac{\mu_0}{4\pi}\int_W \frac{i\mathrm{d}\boldsymbol{l}\times\boldsymbol{r}}{r^3} = -i\frac{\mu_0}{4\pi}\int_W \frac{\boldsymbol{r}\times\mathrm{d}\boldsymbol{l}}{r^3} \tag{23}$$

On the other hand, as shown in Fig. 3 B, if we have a magnetic dipole placed at the point $\boldsymbol{r}$, then this will generate a vector potential at the point of $\mathrm{d}\boldsymbol{l}$ given by

$$\boldsymbol{A}(\boldsymbol{r}') = \frac{\mu_0}{4\pi}\frac{\boldsymbol{m}\times\boldsymbol{r}'}{r'^3} = -\frac{\mu_0}{4\pi}\frac{\boldsymbol{m}\times\boldsymbol{r}}{r^3}, \tag{24}$$

where we have made use of $\boldsymbol{r}' = -\boldsymbol{r}$. The magnetic field due to the vector potential $\boldsymbol{A}$ is given by

$$\boldsymbol{B}_s = \mathrm{rot}\boldsymbol{A}, \tag{25}$$

where we have used the subscript s to indicate that this field originates from the sample. We can calculate the induced voltage using Faraday's law of induction

$$\tilde{V} = -\frac{\mathrm{d}\Phi}{\mathrm{d}t} = -\frac{\mathrm{d}}{\mathrm{d}t}\iint_{\mathrm{Area}} \boldsymbol{B}_s\cdot\mathrm{d}\boldsymbol{a}, \tag{26}$$

where $\mathrm{d}\boldsymbol{a}$ is the surface element. Now we insert Eq. (25), use Stokes' theorem, insert expression (24) for $\boldsymbol{A}$, and rearrange using the cyclic relation $(\boldsymbol{a}\times\boldsymbol{b})\cdot\boldsymbol{c} = (\boldsymbol{b}\times\boldsymbol{c})\cdot\boldsymbol{a}$:

$$\tilde{V} = -\frac{\mathrm{d}}{\mathrm{d}t}\iint_{\mathrm{Area}} \mathrm{rot}\boldsymbol{A}\cdot\mathrm{d}\boldsymbol{a} = -\frac{\mathrm{d}}{\mathrm{d}t}\int_C \boldsymbol{A}\cdot\mathrm{d}\boldsymbol{l} \tag{27}$$

$$= \frac{\mathrm{d}}{\mathrm{d}t}\frac{\mu_0}{4\pi}\int_C \frac{\boldsymbol{m}\times\boldsymbol{r}}{r^3}\cdot\mathrm{d}\boldsymbol{l} = \underbrace{\frac{\mathrm{d}}{\mathrm{d}t}\frac{\mu_0}{4\pi}\int_C \frac{\boldsymbol{r}\times\mathrm{d}\boldsymbol{l}}{r^3}}_{=-\boldsymbol{B}_1/i}\cdot\boldsymbol{m} \tag{28}$$

$$= -\frac{\mathrm{d}}{\mathrm{d}t}\frac{1}{i}\boldsymbol{B}_1\cdot\boldsymbol{m} \tag{29}$$

Now recall that magnetization is defined as magnetic moment per unit volume. Thus, to get the voltage for *all* magnetic moments, we replace the magnetic moment with the magnetization, and integrate over the volume.

$$\tilde{V} = -\frac{\mathrm{d}}{\mathrm{d}t}\frac{1}{i}\iiint \boldsymbol{B}_1\cdot\boldsymbol{M}\mathrm{d}V \tag{30}$$

This is the principle of reciprocity: The voltage induced in the coil by a precessing magnetic moment increases with increasing field generated by the coil at the place of the precessing magnetic moment.

Now we assume that the product of magnetization and magnetic field is constant across the sample volume V_S and vanishes outside the coil. If the magnetization precesses in the transverse plane according to $M_x = M_0\cos(\omega t)$, we get

$$\tilde{V} = \frac{B_1}{i}\omega M_0 V_S\sin(\omega t), \tag{31}$$

The signal amplitude in time is therefore

$$\tilde{V} = \frac{B_1}{i}\omega M_0 V_S \tag{32}$$

Since a good detector will have a homogeneous B_1 across the sample, it can be seen that the signal scales exactly as *magnetic field per current*.

Now we follow Slichter [14] and estimate the amplitude of B_1 for a solenoid and a given radio-frequency power. An inductor carrying a current i stores an energy

$$\frac{1}{2}Li^2. \tag{33}$$

But this energy is really the energy of the field that is produced by the current, so we may write

$$\frac{1}{2}Li^2 = \frac{1}{2}\iiint \boldsymbol{M}\boldsymbol{B}\mathrm{d}V = \frac{1}{2\mu_0}B^2V_c \tag{34}$$

where we assume that the field is homogeneous and contained in the coil with volume V_c. This assumption is valid for an infinite solenoid. Short solenoids generate significant field strength outside of the coil and additionally exhibit B_1 inhomogeneity. We found that for coils with few turns B_1 may be a factor two smaller than the estimate of Eq. (34).

In steady state, the power dissipated in the coil's resistance r_c equals the power provided by the RF amplifier. We therefore have

$$\frac{1}{2}r_c i^2 = P. \tag{35}$$

Substituting this into Eq. (34), we get

$$\frac{1}{2}L\frac{2P}{r_c} = \frac{1}{2\ \mu_0}B^2V_c. \tag{36}$$

Now we introduce the coil's Q factor, $Q = \omega L/r_c$, and solve for B:

$$B = \sqrt{\frac{2QP\mu_0}{\omega V_c}}. \tag{37}$$

The field generated by the coil is linearly polarized, and has to be decomposed into two counter-rotating circularly polarized fields, e.g.

$$B\cos(\omega t) = B_1\exp(j\omega t) + B_1\exp(-j\omega t). \tag{38}$$

Therefore

$$B_1 = B/2 = \sqrt{\frac{\mu_0 QP}{2\omega V_c}}. \tag{39}$$

As we describe in detail in Appendix C, Q is readily measured by the width of the return loss spectrum (i.e. the S_{11} trace on a network analyzer) 3 dB or 7 dB below the baseline [23]. Experimentally, the B_1 amplitude can of course be determined using a nutation experiment. If the duration of a $\pi/2$ pulse is τ, then $|\omega_1|\tau = \pi/2$. Rearranging $\omega_1 = -\gamma B_1$, we get $B_1 = \pi/(2\gamma\tau)$. It is common in the NMR community to drop γ from the denominator and specify the strength of B_1 in kHz. Note that the above equation may be rearranged as

$$\frac{B_1}{\sqrt{P}} = \sqrt{\frac{\mu_0 Q}{2\omega V_c}}, \tag{40}$$

a probe that achieves a stronger B_1 for a given power and volume will have a higher Q and therefore higher sensitivity [24].

If we insert (39) into the expression for the signal amplitude (32), and define the filling factor $\eta = V_s/V_c$, we obtain

$$\tilde{V} = \sqrt{\frac{\mu_0 QP}{2\omega V_c}}\frac{\omega M_0 V_s}{i} = \sqrt{\frac{\mu_0 Q\omega V_c r_c}{2}}\eta M_0 \tag{41}$$

5. The noise

The noise in the coil is Johnson Noise [25], with an amplitude

$$\tilde{V}_n = \sqrt{4 r_c k T_c \Delta f}, \tag{42}$$

where Δf is the bandwidth, T_c is the coil temperature, and r_c is the (frequency-dependent) resistance of the coil. We note that saline solutions effectively increase the coil's resistance at high frequencies [26].

6. The signal-to-noise ratio in the time domain

The signal-to-noise ratio in the time domain is simply the ratio of Eqs. (41) and (42). If we also insert the expression for the magnetization (18), we get

$$\mathrm{SNR}_t = \frac{\tilde{V}}{\tilde{V}_n} = \sqrt{\frac{\mu_0 Q \omega V_c}{8 k T_c \Delta f}} \eta n \gamma \hbar I P. \tag{43}$$

The bandwidth Δf is given by the required bandwidth needed to detect all signals in the spectrum. The Q factor should be as high as possible given the expected bandwidth of the NMR signal. As an example, ^{13}C has a chemical shift range of 200 ppm, corresponding to 20 kHz in a 9.4 T magnet. To avoid non-linearities due to the circuit, we might choose a lower circuit bandwidth limit of 200 kHz, resulting in a $Q \sim 100\ \mathrm{MHz}/200\ \mathrm{kHz} = 500$. A second limitation is imposed by the onset of circuit non-linearity in the form of radiation damping where the signal induced by the precessing magnetization is so strong that it acts back on the magnetization [27]. Radiation-damping causes linebroadening and is readily observed on samples that exhibit a large magnetization either because they contain high-γ nuclei in high concentration (aqueous samples) or because the spins are hyperpolarized. We note that high Q circuits may not only give rise to radiation damping but also to rasing, a technique that can *increase* the sensitivity of detecting signals in a narrow bandwidth [28–32].

It should be noted that the signal-to-noise ratio can only degrade as the signal is amplified by the preamplifier, and processed and digitized by the NMR receiver. For a detailed discussion of the NMR receiver, we refer to the works by Hoult [33] and more recently, by Takeda and Michal [34,35].

7. The signal-to-noise ratio in the frequency domain

Clearly, the signal-to-noise ratio in time is not the same as the signal-to-noise ratio in the frequency domain. We shall calculate the latter using the discrete Fourier transform. The noise in the frequency domain is readily obtained from Parseval's Theorem, which relates the RMS amplitudes in the two domains. We follow the convention of using x_m for samples in the time domain, and X_k for samples in the frequency domain. Parseval's Theorem states that

$$\sum_{m=0}^{N-1} |x_m|^2 = \frac{1}{N} \sum_{k=0}^{N-1} |X_k|^2. \tag{44}$$

where N is the number of points in either domain. Therefore, if the RMS noise is $\tilde{V}_N$ in the time domain, than the RMS noise is $\sqrt{N}\tilde{V}_N$ in the frequency domain. Other things being equal, doubling the number of samples in the time-domain leads to an increase of the RMS noise in the frequency domain by $\sqrt{2}$.

The X_k are the Fourier coefficients, defined as

$$X_k = \sum_{m=0}^{N-1} x_m \exp(-\mathrm{i} 2\pi k m / N). \tag{45}$$

We now assume our signal to appear on resonance, i.e. at $k = 0$, and to decay exponentially with a transverse relaxation rate constant R_2, i.e.

$$x_m = S_0 \exp(-R_2\ m T_A / N) = S_0 \exp(-R_2 T_A / N)^m \tag{46}$$

where T_A is the total acquisition time, so that T_A/N is the dwell time. Then the maximum in the frequency domain appears at $k = 0$, with

$$X_0 = S_0 \sum_{m=0}^{N-1} \exp(-R_2 T_A/N)^m \approx S_0 \sum_{m=0}^{\infty} \exp(-R_2 T_A/N)^m \tag{47}$$

where we have assumed that our signal has decayed at the end of the acquisition time, such that we can approximate the finite series with an infinite geometric series. Since, the series is convergent with $\sum_\infty q^n = 1/(1-q)$, we have

$$X_0 = \frac{S_0}{1 - \exp(-R_2 T_A/N)} \approx \frac{S_0 N}{R_2 T_A}, \tag{48}$$

where we have made use of $N \gg R_2 T_A$ to expand the exponential. The signal-to-noise ratio in the frequency domain can now be written as

$$\mathrm{SNR}_\omega = \frac{S_0 N/(R_2 T_A)}{V_n \sqrt{N}} = \mathrm{SNR}_t \frac{\sqrt{N}}{R_2 T_A} = \sqrt{\frac{\mu_0 Q \omega V_C}{8 k T_c}} \frac{\eta M_0}{R_2 \sqrt{T_A}}. \tag{49}$$

We have used the fact that the bandwidth Δf is the inverse of the dwell time, i.e., $\Delta f = N/T_A$.

Often in NMR we choose to set the acquisition time sufficiently long, such that the NMR signal has decayed completely, and we then use apodization to improve the signal-to-noise ratio. Let R_A be the rate constant of the exponential apodization. Since both the signal and the noise are subjected to apodization, they both decrease. Apodization rescales the signal in the frequency domain by a factor $R_2/(R_2 + R_A)$. The noise in the frequency domain on the other hand is scaled by a factor $\sqrt{\left(1 - \exp\left(-R_A T_A\right)\right) / \left(R_A T_A\right)}$. The signal-to-noise ratio then is

$$\mathrm{SNR}_\omega^{ap} = \sqrt{\frac{\mu_0 Q \omega V_C}{8 k T_c}} \frac{\eta M_0}{(R_2 + R_A)\sqrt{T_A}} \sqrt{\frac{R_A T_A}{1 - \exp(-R_A T_A)}} \tag{50}$$

A typical choice for apodization is the linewidth itself, i.e. $R_A = R_2$. Then, if the apodization is sufficiently strong such that $R_A T_A \gg 1$, we have $1 - \exp\left(-R_A T_A\right) \approx 1$ and the signal-to-noise ratio becomes

$$\mathrm{SNR}_\omega^{ap} = \sqrt{\frac{\mu_0 Q \omega V_C}{8 k T_c}} \frac{\eta M_0}{2\sqrt{R_2}}. \tag{51}$$

We can improve the SNR by repeating our experiment. We assume that also for hyperpolarized signals, the signal adds linearly with every experiment, whereas the noise again grows only with the square root of the number of repetitions. If we give ourselves a total time T_{tot} which is an arbitrary multiple of the time required to do the experiment T_{exp}, then we have

$$\mathrm{SNR}_\omega^{ap,av} = \mathrm{SNR}_\omega \sqrt{\frac{T_{\mathrm{tot}}}{T_{\mathrm{exp}}}} = \sqrt{\frac{\mu_0 Q \omega V_C}{8 k T_c}} \frac{\eta M_0}{2\sqrt{R_2}} \sqrt{\frac{T_{\mathrm{tot}}}{T_{\mathrm{exp}}}} \tag{52}$$

Experimentally, the signal-to-noise ratio is determined by dividing the amplitude of a given signal by the RMS of the noise.[1]

8. Sensitivity and hyperpolarized time gain

In NMR we typically distinguish concentration sensitivity and mass sensitivity. We will get to these terms in a minute. However before doing so, we note that what we really mean with sensitivity is information gain per time. The cost of operating an instrument is linear in time as well, so we could also say that we are interested in information gain per buck. The total time required to achieve a given SNR scales, of course, with the square of the single scan signal-to-noise ratio. If we want to achieve a signal-to-noise ratio of X, then we have

$$T_{\mathrm{tot}} = X^2 \frac{8 k T_c}{\mu_0 Q \omega V_c} \frac{4 R_2}{\eta^2 M_0^2} T_{\mathrm{exp}} \tag{53}$$

[1] The TopSpin SINO macro does essentially this, however it first performs a linear regression of the selected noise data in order to remove baseline artefacts to first order.

We define the HYperpolarized TIme GAin HYTIGA G as

$$G = \frac{T_{\text{tot}}^{\text{th}}}{T_{\text{tot}}^{\text{hyp}}} \tag{54}$$

If we can reduce the required time by using hyperpolarization ($G > 1$), than doing so will have merit. Sometimes, the argument is made that high magnetic fields are expensive, and that hyperpolarization can save money. The monetary saving is the gain weighted by the cost of running experiments with and without hyperpolarization:

$$C = \frac{T_{\text{tot}}^{\text{th}}}{T_{\text{tot}}^{\text{hyp}}} \frac{\$^{\text{th}}}{\$^{\text{hyp}}} \tag{55}$$

where $\$^{\text{th/hyp}}$ is the cost of thermally polarized and hyperpolarized experiments per unit time. We note that, at an annual depreciation of 10%, even a 10 M$ instrument has an hourly depreciation cost of the order of $ 100. A benchtop instrument on the other hand would be 100 times cheaper, so that it comes in at $ 1/h. Whenever hyperpolarization requires additional staff, with costs of the order of $ 100/h, the implication is that the cost gain is almost always smaller than the time gain. Without stringent automation, staff costs are of course also applicable to otherwise affordable hyperpolarization techniques such as parahydrogen-induced polarization.

The time and cost gain depend critically on whether we need to work with a fixed concentration or with a fixed sample volume or mass. We now discuss the time gain for these two cases.

9. Concentration sensitivity

Sometimes, we are forced to work with limited concentrations, for instance if we want to work at or near physiological concentrations, if we want to determine ligand affinity, or if we are limited by solubility or stability of a protein. Without hyperpolarization, the cost is inversely proportional to the sample volume or coil volume, as long as we get a good filling factor (i.e. $\eta \sim 1$). With hyperpolarization, three things change. The polarization changes by the enhancement ϵ, the time for the experiment changes from T_1 to the time constant of the hyperpolarization experiment T_{hyp}, and R_2 may increase due to poorer resolution in the hyperpolarized experiment. The gain from using hyperpolarization then is

$$G = \frac{T_{\text{tot}}^{\text{th}}}{T_{\text{tot}}^{\text{hyp}}} = \frac{R_2^{\text{th}} \epsilon^2}{R_2^{\text{hyp}}} \frac{T_1}{T_{\text{hyp}}} \tag{56}$$

If a hyperpolarization experiment can be carried out at the same rate or even a faster rate than T_1 than one only needs a very modest enhancement or even no enhancement to obtain $G > 1$. This condition is often fulfilled to good approximation in MAS-DNP [36]. It may also be achieved in certain applications of SABRE [37,38] and Overhauser-DNP [39].

On the other hand, in a D-DNP experiment, the effective hyperpolarization time can easily be 10,000 times larger than the liquid state T_1. After all, a hyperpolarization time of 10,000 s corresponds to > 8 experiments/day. Then, if T_1 is of the order of a second, even if $R_2^{\text{hyp}} \sim R_2^{\text{th}}$, one requires enhancements of > 100 to justify hyperpolarization. Recent deuterium-based metabolic imaging studies make stringent use of the short T_1 of ^{2}H and illustrate this fact succinctly [40,41].

10. Mass sensitivity

If we are interested in mass sensitivity, that is, we want to obtain a signal from a small amount of sample, the analysis is rather different. It is well known that for small samples one needs to adapt the coil volume to the available sample. As was shown already in the 90s [42], and in the early 2000s for MAS [43] doing so rigorously enables a detection of a few nL or tens of nanograms of material within minutes *without* hyperpolarization. Microcoils are required to detect such minute amounts of sample without hyperpolarization and we refer to Refs. [44–46] for further reading on this fascinating field.

If we have a limited mass, than we will also have a limited volume, and – for the most sensitive acquisition – we choose our coil volume to match the sample volume. The normal sensitivity is then given by (53).

Now, if we hyperpolarize and dissolve the material, we get a dilution factor D, a possibly different R_2^{hyp} and a different coil volume V_c^{hyp}. If we produce more solvent than needed to fill the available coil volume, we can take that into account using a penalty factor $p <= 1$.

The gain then is

$$G = \frac{T_{\text{tot}}^{\text{th}}}{T_{\text{tot}}^{\text{hyp}}} = p \frac{V_c^{\text{hyp}}}{V_c^{\text{th}}} \frac{R_2^{\text{th}}}{R_2^{\text{hyp}}} \frac{\epsilon^2}{D^2} \frac{T_1}{T_{\text{hyp}}} \tag{57}$$

If we have a mass-limited sample with a volume in the low nL range, than the dilution factor will easily be 10,000. An enhancement of 10,000 would therefore be canceled by the dilution. There would still be a gain from the volume factor, however that gain is readily offset by the time factor. Dissolution-DNP is therefore at present not a viable tool for sensitivity enhancements of samples with volumes in the low nL range.

In more favorable cases the available mass and volume are larger, so that the dilution is only 10–100 fold. In bullet-DNP [24,47–51] one may achieve only 10-fold dilution for samples down to 30 μL. Using organic solvents, the volume can be chosen to only marginally exceed the coil volume, i.e. $p = 0.8$. Allowing for a deterioration in linewidth by a factor 2, and a hyperpolarization time of 2 h, we get

$$G_b = 0.8 \times 10 \frac{1}{2} \frac{\epsilon^2}{10^2} 17200 = \frac{\epsilon^2}{180000} \tag{58}$$

We then need $\epsilon > 450$ to break even. If the dilution is larger, as may be the case in bullet-DNP experiments involving aqueous solutions, or in dissolution-DNP experiments, where a solvent volume of 1 mL is on the lower end of what has been achieved, we would have $D = 30$ and $p = 0.4$. Then we have

$$G_b = 0.4 \times 30 \frac{1}{2} \frac{\epsilon^2}{30^2} 17200 = \frac{\epsilon^2}{1080000} \tag{59}$$

and we need an enhancement of 1000. Such an enhancement is readily attained for low-γ nuclei such as carbon, but more challenging to achieve on rapidly relaxing high-γ nuclei.

We note that the arguments presented here also apply to SABRE and PHIP. These experiments often work best at concentrations below those which one would use when working at thermal equilibrium.

Of course, many labs do not have a microfluidic detector for every conceivable sample volume, and many of the assumptions that we made can be questioned. After correcting for sample volume, a cryoprobe has a superior performance or Q than a microcoil, and small coils bring about their own challenges with respect to loading, shimming, and so on. For the time being, however, the scaling that we describe here is also observed in experiment, where nanograms can be detected using either small coils [42] or hyperpolarization. The sensitivity of NMR will extend into the picogram range when near unity polarization with little or no dilution becomes available at the nL to low μL scale.

CRediT authorship contribution statement

Karel Kouřil: Writing – original draft, Investigation. **Benno Meier:** Writing – original draft, Investigation, Funding acquisition, Conceptualization.

Declaration of competing interest

The authors declare the following financial interests/personal relationships which may be considered as potential competing interests: B. M. and K. K. are co-founders and owners of HyperSpin Scientific UG.

Acknowledgments

B. M. thanks Jürgen Haase for teaching a quantitative way to look at NMR signals many years ago, and Mengjia He for spotting a sign error in an earlier presentation of Hoult and Richard's principle of reciprocity. This work has been supported by the "Impuls- und Vernetzungsfonds of the Helmholtz-Association" (grant VH-NG-1432), by the European Research Council (ERC) under the European Union's Horizon 2020 research and innovation programme (grant agreement No 951459 HiSCORE), and by the Deutsche Forschungsgemeinschaft (DFG, grant number 454252029 - SFB 1527).

Appendix A. The Brillouin function

The general definition of the spin polarization is:

$$P = \frac{1}{I}\left\langle \hat{I}_z \right\rangle \tag{A.1}$$

where

$$\left\langle \hat{I}_z \right\rangle = \sum_{m=-I}^{I} m p_m \tag{A.2}$$

The probability of the mth Zeeman level being occupied is given by

$$p_m = \frac{1}{Z}\sum_{m=-I}^{I} m \exp\left(-\frac{E_m}{kT}\right). \tag{A.3}$$

Here, Z is the partition sum, which, with $E_m = -m\hbar\gamma B_0$ and $x = \frac{\hbar\gamma B_0}{kT}$ is

$$Z = \sum_{m=-I}^{I} \exp\left(-\frac{E_m}{kT}\right) = \sum_{m=-I}^{I} \exp(mx). \tag{A.4}$$

Evaluation of this finite sum using the geometric series (and index shifting) gives

$$Z = \frac{e^{-Ix} - e^{(I+1)x}}{1 - e^{x}}, \tag{A.5}$$

which we rewrite as

$$Z = \frac{\sinh((I+\frac{1}{2})x)}{\sinh(\frac{1}{2}x)} \tag{A.6}$$

Note that the expectation value of $\hat{I}_z$, (A.2) is the derivative of $\ln Z$:

$$\left\langle \hat{I}_z \right\rangle = \frac{1}{Z}\sum_{m=-I}^{I} m\exp(mx) = \frac{\mathrm{d}}{\mathrm{d}x}\ln Z \tag{A.7}$$

Inserting the result for Z, (A.6), we obtain:

$$\begin{aligned}\frac{\mathrm{d}\ln Z}{\mathrm{d}x} &= \frac{1}{Z}\frac{\mathrm{d}Z}{\mathrm{d}x}\\ &= \frac{\sinh(\frac{1}{2}x)}{\sinh(\frac{2I+1}{2}x)}\,\frac{\frac{2I+1}{2}\cosh(\frac{2I+1}{2}x)\sinh(\frac{1}{2}x) - \frac{1}{2}\sinh(\frac{2I+1}{2}x)\cosh(\frac{1}{2}x)}{\sinh^2\left(\frac{1}{2}x\right)}\\ &= \frac{2I+1}{2}\coth\left(\frac{2I+1}{2}x\right) - \frac{1}{2}\coth\left(\frac{1}{2}x\right)\end{aligned} \tag{A.8}$$

Finally we arrive at the following expression for the polarization:

$$P = \frac{2I+1}{2I}\coth\left(\frac{2I+1}{2}x\right) - \frac{1}{2I}\coth\left(\frac{1}{2}x\right) = B_I(Ix). \tag{A.9}$$

Here, B_I is known as the Brillouin function:

$$B_I(y) := \frac{2I+1}{2I}\coth\left(\frac{2I+1}{2I}y\right) - \frac{1}{2I}\coth\left(\frac{1}{2I}y\right). \tag{A.10}$$

Expanding x, we get

$$P = B_I\left(\frac{I\hbar\gamma B_0}{kT}\right). \tag{A.11}$$

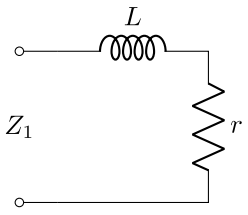

Fig. C.4. The RF coil is a lossy inductor that we model as a series circuit of an ideal inductor L and a resistor r.

For the case of $I = 1/2$ the Brillouin function simplifies to the tanh expression:

$$\begin{aligned}B_{1/2}(y) &= 2\coth(2y) - \coth(y)\\ &= 2\frac{\cosh 2y}{\sinh 2y} - \frac{\cosh y}{\sinh y}\\ &= 2\frac{2\cosh^2 y - 1}{2\sinh y\cosh y} - \frac{\cosh y}{\sinh y}\\ &= \frac{\cosh^2 y - 1}{\sinh y\cosh y}\\ &= \tanh y = \tanh(Ix) = \tanh\left(\frac{\hbar\gamma B_0}{2kT}\right)\end{aligned} \tag{A.12}$$

By expanding the Brillouin function using the approximation $\coth x \approx \frac{1}{x} + \frac{x}{3}$ and using $M_z = n\gamma\hbar IP$, one again obtains the Curie law Eq. (19).

Appendix B. Polarization tensors for spins ≥ 1

One can define spin polarization operators [52,53] $\hat{T}_{LM}(I)$ with rank $L = 0, 1, \ldots, 2I$ and $M = -L, -L+1, \ldots, L$. The rank 0 operator is a scalar which conveys no useful information, the rank 1 operator is the familiar polarization vector. The higher rank polarization tensors are necessary for nuclei with spin $I > 1/2$.

Consider the case of spin $I = 1$ nuclei in a magnetic field parallel to the z axis and denote the relative populations of the three Zeeman levels ($m_I = -1, 0, 1$) as p_{m_I}. Since $p_{-1}+p_0+p_1 = 1$ there are two degrees of freedom and we can describe the order using two numbers [54,55]: vector polarization P and tensor polarization P_{zz}:

$$P = p_1 - p_{-1} \tag{B.1}$$

$$P_{zz} = 1 - 3p_0 \tag{B.2}$$

Appendix C. Coil Q and return loss

We discuss a simple resonant circuit as it is used in NMR and calculate its return loss. We then derive expressions for the coil Q from the return loss of an equivalent series RCL circuit. The return loss is readily measured with a vector network analyzer (VNA). There are several historical articles in the literature that describe how Q can be measured without a VNA, however thanks to the advent of very affordable VNAs like the NanoVNA, today every lab can afford quantitative measurements of the return loss. Throughout this section we give general formulas, but we also evaluate them for a specific coil so that readers can validate their own implementation of the equations. There are many ways to tune a coil, and we refer to Refs. [56–60] for further reading on this subject.

The RF coil is a lossy inductor which we model as a series circuit of an ideal inductor L and a resistor r. For our specific example we choose $r = 1\ \Omega$ and $L = 100$ nH. The impedance of the coil is

$$Z_1 = j\omega L + r. \tag{C.1}$$

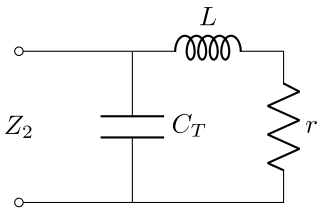

Fig. C.5. The RF coil and the tuning capacitor. The tuning capacitor is chosen such that the real part of the input impedance is $\Re(Z_2(\omega_0)) = 50\,\Omega$.

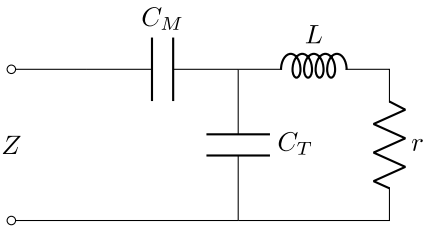

Fig. C.6. The tuned and matched coil with impedance Z.

We also choose our resonance frequency to be 100 MHz, so $\omega_0 = 2\pi 100$ MHz. The impedance of the lossy coil at 100 MHz is then $(1+j63)\,\Omega$. Our model of the coil is shown in Fig. C.4. In practice one often does not have good *a priori* knowledge of L and r. One can then use a parallel capacitor of known value and a sniffer loop to determine L [58]. The resistance (at the desired frequency) can be determined from the return loss as we will now show.

To transfer energy in and out of the coil, we need to match its impedance to the system impedance of the spectrometer, which is $Z_0 = 50\,\Omega$. In a sense, this is the principle of reciprocity again, however this time we are dealing with source and load impedances. Power transfer into- and out of the load is maximal when the source and load impedances are matched [61]. As a side note, the available "signal power" of a matched NMR circuit is dissipated in equal amounts by the coil loss and the input impedance of the receiver. Doubling the losses in the circuit halves the Q - the loaded Q (when connected to the receiver) is half the unloaded Q [57]. Now in order to match the impedance, we will first add a shunt capacitor, whose job it is to change the real part of the impedance to $50\,\Omega$.

Let C_T be the capacitance of the shunt tuning capacitor. Its impedance is then $Z_T = 1/(j\omega C_T)$. The impedance looking at the coil via the shunt capacitor is (see Fig. C.5)

$$Z_2 = \frac{Z_T Z_1}{Z_T + Z_1}. \tag{C.2}$$

By inserting the expressions for Z_T and Z_1, and extending with the complex conjugate we get the following expression for the real part of Z_2:

$$\Re Z_2 = \frac{rL/C_T - rb/(\omega_0 C_T)}{r^2 + b^2}, \tag{C.3}$$

with $b = \omega_0 L - 1/(\omega_0 C_T)$. We now solve the quadratic equation $\Re Z_2 = Z_0$ for C_T and obtain, after some simplification

$$C_T = \frac{1}{r^2 + (\omega_0 L)^2}\left(L \pm \sqrt{\frac{r\omega_0 L^2 - Z_0 r^2 + r^3}{\omega_0^2 Z_0}}\right) \tag{C.4}$$

We chose the smaller value for C_T, i.e. to subtract the square root. For experts, this choice means that we will move a shorter distance on the Smith chart, and retain a positive reactance, i.e. one that we can cancel with a series matching capacitor. For our example, we get $C_T = 21.8$ pF. Now we need to cancel the remaining reactance with a matching capacitor C_M, i.e.

$$\frac{1}{j\omega C_M} + j\Im Z_2 = 0 \Leftrightarrow C_M = \frac{1}{\omega_0 \Im Z_2} \tag{C.5}$$

For our example we get $C_M = 3.6$ pF.

Now we have completed our RF circuit, as shown in C.6. Since we know the values for all components, we can calculate its impedance at any frequency ω as

$$Z = \frac{1}{j\omega C} + \frac{(j\omega L + r)\frac{1}{j\omega C_T}}{j\omega L + r + 1/(j\omega C_T)}. \tag{C.6}$$

From the impedance we can calculate the reflection coefficient

$$\Gamma = \frac{Z - Z_0}{Z + Z_0} \tag{C.7}$$

and the return loss (RL, in dB) as

$$\mathrm{RL} = -20\log|\Gamma| = -20\log\left|\frac{Z - Z_0}{Z + Z_0}\right| \tag{C.8}$$

To see how the return loss depends on Q, we follow Doty et al. [23] and model our four-component tuned-and matched circuit with an equivalent three-component series RLC circuit as depicted in Fig. C.7.

On resonance, the reactances of a series RLC circuit's coil and capacitor cancel, and the impedance is purely resistive, i.e. $Z_e(\omega_0) = R_e$. Therefore, we have to chose $R_e = Z_0 = 50\,\Omega$.

In order to chose the value for the inductance L_e, we note that the circuit Q factor is defined as [62]:

$$Q = \omega\frac{W_m + W_e}{P_l}, \tag{C.9}$$

where W_m and W_e are the average energies stored in the inductor and capacitor respectively. For a current with effective amplitude i on resonance $W_m = \frac{1}{2}L_e i^2$, and $W_m = W_e$. The losses are $P_l = R_e i^2$ and we obtain on resonance

$$Q = \omega_0\frac{L_e i^2}{R i^2} = \frac{\omega L_e}{R_e} = \frac{\omega L}{r} \Rightarrow L_e = \frac{R_e}{r}L. \tag{C.10}$$

where we have used the fact that $Q = \frac{\omega L}{r}$ applies for the NMR circuit with impedance Z. For our example, $L_e = 50L = 5\,\mu$H. With $\omega_0 = \frac{1}{\sqrt{L_e C_e}}$ we obtain C_e, in our example 0.51 pF.

Now we again know all the component values of the equivalent circuit, and we can compute Z_e at any frequency ω:

$$Z_e = R_e + j\omega L_e + \frac{1}{j\omega C_e}. \tag{C.11}$$

The return losses of the exemplary NMR circuit and the equivalent series circuit are shown in Fig. C.8 A. Notebooks with implementations of the return loss calculations in bare Python and using scikit-rf [63] are available online (see Data availability). While the return loss of both the NMR circuit and the equivalent circuit are almost identical, the same is not at all true for the impedances, shown for both circuits in Fig. C.8 B. However, since power transfer is all we care about, the equivalent series is an excellent model of the NMR circuit. Furthermore, as can be seen in Fig. C.8 B, the real part of Z_e is constant, and the complex part is linear to a very good approximation.

We can therefore expand Eq. (C.11) into a series at $\omega = \omega_0$ [62]. Clearly, for the zero order term $Z_e(\omega_0) = R_e = Z_0$. For the first order term we obtain

$$\left.\frac{\partial Z_e}{\partial\omega}\right|_{\omega_0}(\omega - \omega_0) = jL_e(\omega - \omega_0) - \frac{1}{j\omega_0^2 C_e}(\omega - \omega_0) = j2L_e(\omega - \omega_0), \tag{C.12}$$

where we have used $\omega_0^2 L_e C_e = 1$. Our approximation is therefore

$$Z_e \approx Z_0 + j2L_e(\omega - \omega_0) = Z_0 + j2L_e\epsilon, \tag{C.13}$$

where we have introduced $\epsilon = \omega - \omega_0$.

From this expression one can derive two ways to measure Q, and we now show that they are equivalent.

The "3 dB technique" uses the width of the return line at 3 dB. We then have

$$3 = -20\log|\Gamma| \Leftrightarrow |\Gamma|^2 = \frac{1}{2}. \tag{C.14}$$

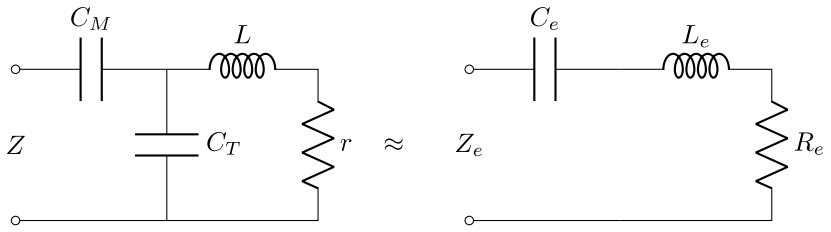

Fig. C.7. The NMR circuit (left) and its equivalent series RLC circuit with components R_e, L_e and C_e.

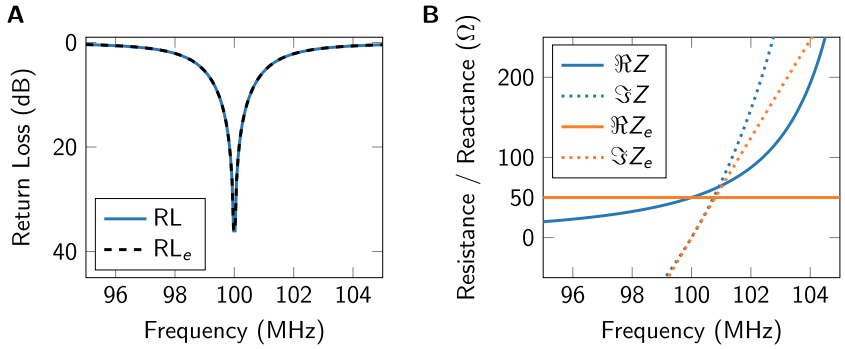

Fig. C.8. (**A**) Return loss of the NMR circuit (blue), and its equivalent series RCL circuit (dashed, black). As can be seen, the correspondence is excellent. (**B**) Real and imaginary part of the impedance of the NMR circuit (blue solid and blue dotted line respectively), and real and imaginary part of the impedance of the equivalent RCL circuit (orange solid and orange dotted line respectively). The impedance of the equivalent circuit Z_e is readily described using a first order expansion.

But we also have

$$|\Gamma|^2 = \left|\frac{Z - Z_0}{Z + Z_0}\right|^2 \approx \left|\frac{Z_e - Z_0}{Z_e + Z_0}\right|^2 = \left|\frac{j2L_e\epsilon}{2Z_0 + j2L_e\epsilon}\right|^2 = \frac{(\epsilon L_e)^2}{Z_0^2 + (\epsilon L_e)^2} = \frac{1}{2} \tag{C.15}$$

This equation is fulfilled when $\epsilon L_e = Z_0$. The 3 dB bandwidth is $\Delta\omega_{3\text{dB}} = 2(\omega - \omega_0) = 2\epsilon$, so that we get

$$\frac{\Delta\omega_{3\text{dB}}}{2} = \frac{Z_0}{L_e}\frac{\omega_0}{\omega_0} = \frac{\omega_0}{Q} \Rightarrow Q = \frac{2\omega_0}{\Delta\omega_{3\text{dB}}}. \tag{C.16}$$

The alternative "7 dB technique", described by Doty et al. [23], chooses ϵ such that $2L_e\epsilon = \pm Z_0 = \pm R_e$. For these two values of ϵ, the real and imaginary parts are equal in magnitude, i.e. $Z_e = Z_0(1 \pm j)$, and their phase differs by 90 degree. We have

$$|\Gamma|^2 = \left|\frac{Z - Z_0}{Z + Z_0}\right|^2 \approx \left|\frac{\pm j}{2 \pm j}\right|^2 = \frac{1}{5} \tag{C.17}$$

and the return loss is

$$\text{RL} = -20\log|\Gamma| = -10\log|\Gamma|^2 = -10\log(0.2) = 6.99\,\text{dB} \approx 7\,\text{dB}. \tag{C.18}$$

Again, the 7 dB bandwidth equals 2ϵ, so that

$$\Delta\omega_{7\text{dB}} = 2\epsilon = \frac{R_e}{L_e} = \omega_0\frac{R_e}{\omega_0 L_e} = \frac{\omega_0}{Q} \Rightarrow Q = \frac{\omega_0}{\Delta\omega_{7\text{dB}}} \tag{C.19}$$

We usually work with the 7 dB technique since it evaluates the return loss closer to resonance.

Data availability

Notebooks with implementations of the return loss calculations in bare Python and using scikit-rf [63] (Arsenovic et al., 2022) are available in KITopen at https://doi.org/10.35097/st1kjwpvsce77dhw.

References

[1] D.T. Peat, M.L. Hirsch, D.G. Gadian, A.J. Horsewill, J.R. Owers-Bradley, J.G. Kempf, Low-field thermal mixing in [1-^{13}C] pyruvic acid for brute-force hyperpolarization, Phys. Chem. Chem. Phys. 18 (28) (2016) 19173–19182, http://dx.doi.org/10.1039/c6cp02853e.

[2] M.L. Hirsch, N. Kalechofsky, A. Belzer, M. Rosay, J.G. Kempf, Brute-force hyperpolarization for NMR and MRI, J. Am. Chem. Soc. 137 (26) (2015) 8428–8434, http://dx.doi.org/10.1021/jacs.5b01252.

[3] A.W. Overhauser, Polarization of nuclei in metals, Phys. Rev. 92 (2) (1953) 411–415, http://dx.doi.org/10.1103/physrev.92.411.

[4] T.R. Carver, C.P. Slichter, Experimental verification of the Overhauser nuclear polarization effect, Phys. Rev. 102 (1956) 975–980, http://dx.doi.org/10.1103/PhysRev.102.975.

[5] E. Ravera, C. Luchinat, G. Parigi, Basic facts and perspectives of Overhauser DNP NMR, J. Magn. Reson. 264 (nil) (2016) 78–87, http://dx.doi.org/10.1016/j.jmr.2015.12.013.

[6] M. Bennati, T. Orlando, Overhauser DNP in liquids on ^{13}C nuclei, in: EMagRes, John Wiley & Sons, 2019, pp. 11–18, http://dx.doi.org/10.1002/9780470034590.emrstm1563.

[7] R. Kaptein, J. Oosterhoff, Chemically induced dynamic nuclear polarization Ii, Chem. Phys. Lett. 4 (4) (1969) 195–197, http://dx.doi.org/10.1016/0009-2614(69)80098-9.

[8] M.A. Bouchiat, T.R. Carver, C.M. Varnum, Nuclear polarization in He^3 gas induced by optical pumping and dipolar exchange, Phys. Rev. Lett. 5 (1960) 373–375, http://dx.doi.org/10.1103/PhysRevLett.5.373.

[9] J. Matysik, A. Diller, E. Roy, A. Alia, The solid-state photo-CIDNP effect, Photosynth. Res. 102 (2009) 427–435.

[10] J.H. Lee, A. Sekhar, S. Cavagnero, ^{1}H-detected ^{13}C photo-CIDNP as a sensitivity enhancement tool in solution NMR, J. Am. Chem. Soc. 133 (21) (2011) 8062–8065, http://dx.doi.org/10.1021/ja111613c.

[11] H. Yang, S. Li, C.A. Mickles, V. Guzman-Luna, K. Sugisaki, C.M. Thompson, H.H. Dang, S. Cavagnero, Selective isotope labeling and LC-photo-CIDNP enable NMR spectroscopy at low-nanomolar concentration, J. Am. Chem. Soc. 144 (26) (2022) 11608–11619, http://dx.doi.org/10.1021/jacs.2c01809.

[12] F. De Biasi, M.A. Hope, C.E. Avalos, G. Karthikeyan, G. Casano, A. Mishra, S. Badoni, G. Stevanato, D.J. Kubicki, J. Milani, J.-P. Ansermet, A.J. Rossini, M. Lelli, O. Ouari, L. Emsley, Optically enhanced solid-state ^{1}H NMR spectroscopy, J. Am. Chem. Soc. 145 (27) (2023) 14874–14883, http://dx.doi.org/10.1021/jacs.3c03937.

[13] J. Eills, D. Budker, S. Cavagnero, E.Y. Chekmenev, S.J. Elliott, S. Jannin, A. Lesage, J. Matysik, T. Meersmann, T. Prisner, J.A. Reimer, H. Yang, I.V. Koptyug, Spin hyperpolarization in modern magnetic resonance, Chem. Rev. 123 (4) (2023) 1417–1551, http://dx.doi.org/10.1021/acs.chemrev.2c00534.

[14] C.P. Slichter, Principles of magnetic resonance, Springer Ser. Solid-State Sci. (1990) http://dx.doi.org/10.1007/978-3-662-09441-9.

[15] C. Kittel, Introduction to Solid State Physics, eighth ed., Wiley, Hoboken, 2005, 680 pages, URL https://bib-pubdb1.desy.de/record/371097.

[16] A. Schweiger, G. Jeschke, Principles of Pulse Electron Paramagnetic Resonance, Oxford University Press, 2005.

[17] A. Abragam, W.G. Proctor, Spin temperature, Phys. Rev. 109 (5) (1958) 1441–1458, http://dx.doi.org/10.1103/physrev.109.1441.

[18] S.F.J. Cox, V. Bouffard, M. Goldman, The coupling of two nuclear Zeeman reservoirs by the electronic spin-spin reservoir, J. Phys. C: Solid State Phys. 6 (5) (1973) http://dx.doi.org/10.1088/0022-3719/6/5/006, L100–L103.
[19] H. Kouřilová, M. Jurkutat, D. Peat, K. Kouřil, A.S. Khan, A.J. Horsewill, J.F. MacDonald, J. Owers-Bradley, B. Meier, Radical-induced hetero-nuclear mixing and low-field ^{13}C relaxation in solid pyruvic acid, Phys. Chem. Chem. Phys. 24 (46) (2022) 28242–28249, http://dx.doi.org/10.1039/d2cp04535d.
[20] M. Jurkutat, H. Kouřilová, D. Peat, K. Kouřil, A.S. Khan, A.J. Horsewill, J.F. MacDonald, J. Owers-Bradley, B. Meier, Radical-induced low-field ^{1}H relaxation in solid pyruvic acid doped with trityl-OX063, J. Phys. Chem. Lett. 13 (44) (2022) 10370–10376, http://dx.doi.org/10.1021/acs.jpclett.2c02357.
[21] M.H. Levitt, C. Bengs, Hyperpolarization and the physical boundary of Liouville space, Magn. Reson. 2 (1) (2021) 395–407, http://dx.doi.org/10.5194/mr-2-395-2021.
[22] D. Hoult, R. Richards, The signal-to-noise ratio of the nuclear magnetic resonance experiment, J. Magn. Reson. 24 (1) (1976) 71–85, http://dx.doi.org/10.1016/0022-2364(76)90233-x.
[23] F. Doty, T. Connick, X. Ni, M. Clingan, Noise in high-power, high-frequency double-tuned probes, J. Magn. Reson. 77 (3) (1988) 536–549, http://dx.doi.org/10.1016/0022-2364(88)90011-x.
[24] P. Narwal, N. Lorz, M. Minaei, S. Jannin, K. Kouřil, A. Gossert, B. Meier, Bullet-DNP enables NMR spectroscopy of pyruvate and amino acids at nanomolar to low micromolar concentrations, Anal. Chem. (2024) http://dx.doi.org/10.1021/acs.analchem.4c00618, (online).
[25] H. Nyquist, Thermal agitation of electric charge in conductors, Phys. Rev. 32 (1) (1928) 110–113, http://dx.doi.org/10.1103/physrev.32.110.
[26] A.E. Kelly, H.D. Ou, R. Withers, V. Dötsch, Low-conductivity buffers for high-sensitivity NMR measurements, J. Am. Chem. Soc. 124 (40) (2002) 12013–12019.
[27] N. Bloembergen, R.V. Pound, Radiation damping in magnetic resonance experiments, Phys. Rev. 95 (1) (1954) 8–12, http://dx.doi.org/10.1103/physrev.95.8.
[28] S. Korchak, L. Kaltschnee, R. Dervisoglu, L. Andreas, C. Griesinger, S. Glöggler, Spontaneous enhancement of magnetic resonance signals using a raser, Angew. Chem. 133 (38) (2021) 21152–21158, http://dx.doi.org/10.1002/ange.202108306.
[29] M. Suefke, S. Lehmkuhl, A. Liebisch, B. Blümich, S. Appelt, Para-hydrogen raser delivers sub-millihertz resolution in nuclear magnetic resonance, Nat. Phys. 13 (6) (2017) 568–572, http://dx.doi.org/10.1038/nphys4076.
[30] E.M.M. Weber, D. Kurzbach, D. Abergel, A DNP-hyperpolarized solid-state water NMR maser: Observation and qualitative analysis, Phys. Chem. Chem. Phys. 21 (38) (2019) 21278–21286, http://dx.doi.org/10.1039/c9cp03334c.
[31] I. Adelabu, S. Nantogma, S. Fleischer, M. Abdulmojeed, H. de Maissin, A.B. Schmidt, S. Lehmkuhl, M.S. Rosen, S. Appelt, T. Theis, C. Qian, E.Y. Chekmenev, Toward ultra-high-quality-factor wireless masing magnetic resonance sensing, Angew. Chem. 63 (37) (2024) e202406551.
[32] V.F.T.J. Chacko, A. Louis-Joseph, D. Abergel, Multimode masers of thermally polarized nuclear spins in solution NMR, Phys. Rev. Lett. 133 (15) (2024) 158001, http://dx.doi.org/10.1103/physrevlett.133.158001.
[33] D. Hoult, The nmr receiver: A description and analysis of design, Prog. Nucl. Magn. Reson. Spectrosc. 12 (1) (1978) 41–77, http://dx.doi.org/10.1016/0079-6565(78)80002-8.
[34] K. Takeda, Opencore NMR: Open-source core modules for implementing an integrated FPGA-based nmr spectrometer, J. Magn. Reson. 192 (2) (2008) 218–229, http://dx.doi.org/10.1016/j.jmr.2008.02.019.
[35] C.A. Michal, A low-cost multi-channel software-defined radio-based NMR spectrometer and ultra-affordable digital pulse programmer, Concepts Magn. Reson. B: Magn. Reson. Eng. 48B (3) (2018) e21401, http://dx.doi.org/10.1002/cmr.b.21401, arXiv:https://onlinelibrary.wiley.com/doi/pdf/10.1002/cmr.b.21401.
[36] B. Corzilius, High-field dynamic nuclear polarization, Annu. Rev. Phys. Chem. 71 (1) (2020) 143–170, http://dx.doi.org/10.1146/annurev-physchem-071119-040222.
[37] R.W. Adams, J.A. Aguilar, K.D. Atkinson, M.J. Cowley, P.I.P. Elliott, S.B. Duckett, G.G.R. Green, I.G. Khazal, J. Lopez-Serrano, D.C. Williamson, Reversible interactions with para-hydrogen enhance NMR sensitivity by polarization transfer, Science 323 (5922) (2009) 1708–1711, http://dx.doi.org/10.1126/science.1168877.
[38] L. Sellies, R.L.E.G. Aspers, M.C. Feiters, F.P.J.T. Rutjes, M. Tessari, Parahydrogen hyperpolarization allows direct NMR detection of α-amino acids in complex (bio)mixtures, Angew. Chem. 133 (52) (2021) 27160–27165, http://dx.doi.org/10.1002/ange.202109588.
[39] T. Orlando, R. za Dervişoğlu, M. Levien, I. Tkach, T.F. Prisner, L.B. Andreas, V.P. Denysenkov, M. Bennati, Dynamic nuclear polarization of ^{13}C nuclei in the liquid state over a 10 Tesla field range, Angewandte Chemie International Edition 58 (5) (2018) 1402–1406, http://dx.doi.org/10.1002/anie.201811892.
[40] J.C.M. Low, A.J. Wright, F. Hesse, J. Cao, K.M. Brindle, Metabolic imaging with deuterium labeled substrates, Prog. Nucl. Magn. Reson. Spectrosc. 134–135 (2023) 39–51, http://dx.doi.org/10.1016/j.pnmrs.2023.02.002.
[41] E.T. Montrazi, K. Sasson, L. Agemy, A. Scherz, L. Frydman, Molecular imaging of tumor metabolism: Insight from pyruvate- and glucose-based deuterium MRI studies, Sci. Adv. 10 (11) (2024) http://dx.doi.org/10.1126/sciadv.adm8600.
[42] D.L. Olson, T.L. Peck, A.G. Webb, R.L. Magin, J.V. Sweedler, High-resolution microcoil ^{1}H-NMR for mass-limited, nanoliter-volume samples, Science 270 (5244) (1995) 1967–1970, http://dx.doi.org/10.1126/science.270.5244.1967.
[43] D. Sakellariou, G.L. Goff, J.-F. Jacquinot, High-resolution, high-sensitivity NMR of nanolitre anisotropic samples by coil spinning, Nature 447 (7145) (2007) 694–697, http://dx.doi.org/10.1038/nature05897.
[44] V. Badilita, R.C. Meier, N. Spengler, U. Wallrabe, M. Utz, J.G. Korvink, Microscale nuclear magnetic resonance: a tool for soft matter research, Soft Matter 8 (41) (2012) 10583, http://dx.doi.org/10.1039/c2sm26065d.
[45] P. van Bentum, J. Janssen, A. Kentgens, J. Bart, J. Gardeniers, Stripline probes for nuclear magnetic resonance, J. Magn. Reson. 189 (1) (2007) 104–113, http://dx.doi.org/10.1016/j.jmr.2007.08.019.
[46] A. Webb, Radiofrequency microcoils for magnetic resonance imaging and spectroscopy, J. Magn. Reson. 229 (2013) 55–66, http://dx.doi.org/10.1016/j.jmr.2012.10.004.
[47] K. Kouřil, H. Kouřilová, S. Bartram, M.H. Levitt, B. Meier, Scalable dissolution-dynamic nuclear polarization with rapid transfer of a polarized solid, Nature Commun. 10 (1) (2019) 1733, http://dx.doi.org/10.1038/s41467-019-09726-5.
[48] K. Kouřil, M. Gramberg, M. Jurkutat, H. Kouřilová, B. Meier, A cryogen-free, semi-automated apparatus for bullet-dynamic nuclear polarization with improved resolution, Magn. Reson. 2 (2) (2021) 815–825, http://dx.doi.org/10.5194/mr-2-815-2021.
[49] J. Fukazawa, Y. Mochizuki, S. Kanai, N. Miura, M. Negoro, A. Kagawa, Real-time monitoring of hydrolysis reactions of pyrophosphates with dissolution dynamic nuclear polarization, J. Phys. Chem. Lett. 15 (28) (2024) 7288–7294, http://dx.doi.org/10.1021/acs.jpclett.4c01456.
[50] I. Katz, A. Schmidt, I. Ben-Shir, M. Javitt, K. Kouřil, A. Capozzi, B. Meier, A. Lang, B. Pokroy, A. Blank, Long-lived enhanced magnetization-a practical metabolic MRI contrast material, Sci. Adv. 10 (28) (2024) http://dx.doi.org/10.1126/sciadv.ado2483.
[51] A. Razanahoera, A. Sonnefeld, K. Sheberstov, P. Narwal, M. Minaei, K. Kouřil, G. Bodenhausen, B. Meier, Hyperpolarization of long-lived states of protons in aliphatic chains by bullet dynamic nuclear polarization, revealed on the fly by spin-lock-induced crossing, J. Phys. Chem. Lett. 15 (35) (2024) 9024–9029, http://dx.doi.org/10.1021/acs.jpclett.4c01457.
[52] D.A. Varshalovich, A.N. Moskalev, V.K. Khersonskii, Quantum Theory of Angular Momentum, WORLD SCIENTIFIC, 1988, http://dx.doi.org/10.1142/0270, arXiv:https://www.worldscientific.com/doi/pdf/10.1142/0270.
[53] Q.-B. Shen, Basic knowledge of polarization theory of nuclear reactions, in: Polarization Theory of Nuclear Reactions, Springer International Publishing, Cham, 2023, pp. 1–22, http://dx.doi.org/10.1007/978-3-031-11878-4.
[54] W. Lakin, Spin polarization of the deuteron, Phys. Rev. 98 (1955) 139–144, http://dx.doi.org/10.1103/PhysRev.98.139.
[55] D. Keller, D. Crabb, D. Day, Enhanced tensor polarization in solid-state targets, Nucl. Instrum. Methods Phys. Res. A 981 (2020) 164504, http://dx.doi.org/10.1016/j.nima.2020.164504, URL https://www.sciencedirect.com/science/article/pii/S0168900220309013.
[56] J.L. Uribe, R.W. Martin, A practical introduction to radio frequency electronics for NMR probe builders, J. Magn. Reson. Open 19 (2024) 100153, http://dx.doi.org/10.1016/j.jmro.2024.100153.
[57] M.S. Conradi, NMR instrumentation - a primer, J. Magn. Reson. Open 12–13 (2022) 100081, http://dx.doi.org/10.1016/j.jmro.2022.100081.
[58] D.D. Wheeler, M.S. Conradi, Practical exercises for learning to construct NMR/MRI probe circuits, Concepts Magn. Reson. A 40A (1) (2012) 1–13, http://dx.doi.org/10.1002/cmr.a.21221.
[59] V.D. Kodibagkar, M.S. Conradi, Remote tuning of NMR probe circuits, J. Magn. Reson. 144 (1) (2000) 53–57, http://dx.doi.org/10.1006/jmre.2000.2052.
[60] J. Mispelter, M. Lupu, A. Briguet, NMR Probeheads For Biophysical And Biomedical Experiments: Theoretical Principles And Practical Guidelines, second ed., World Scientific Publishing Company, 2015, URL https://books.google.de/books?id=Iec7DQAAQBAJ.
[61] J. Hagen, Radio-Frequency Electronics: Circuits and Applications, Cambridge University Press, 2009.
[62] D. Pozar, Microwave Engineering, Wiley, 2012, URL https://books.google.de/books?id=JegbAAAAQBAJ.
[63] A. Arsenovic, J. Hillairet, J. Anderson, H. Forstén, V. Rieß, M. Eller, N. Sauber, R. Weikle, W. Barnhart, F. Forstmayr, Scikit-rf: An open source python package for microwave network creation, analysis, and calibration [speaker's corner], IEEE Microw. Mag. 23 (1) (2022) 98–105, http://dx.doi.org/10.1109/MMM.2021.3117139.